



Multiscale Exploration of Texture and Microstructure Development in Recrystallization Annealing of Heavily Deformed Ferritic Alloys

Yildirim, C.; Mavrikakis, N.; Cook, P. K.; Lamas, R. Rodriguez; Poulsen, H. F.; Detlefs, C.; Kutsal, M.

Published in:
IOP Conference Series-Materials Science and Engineering

Link to article, DOI:
[10.1088/1757-899X/1249/1/012044](https://doi.org/10.1088/1757-899X/1249/1/012044)

Publication date:
2022

Document Version
Publisher's PDF, also known as Version of record

[Link back to DTU Orbit](#)

Citation (APA):
Yildirim, C., Mavrikakis, N., Cook, P. K., Lamas, R. R., Poulsen, H. F., Detlefs, C., & Kutsal, M. (2022). Multiscale Exploration of Texture and Microstructure Development in Recrystallization Annealing of Heavily Deformed Ferritic Alloys. *IOP Conference Series-Materials Science and Engineering*, 1249, Article 012044. <https://doi.org/10.1088/1757-899X/1249/1/012044>

General rights

Copyright and moral rights for the publications made accessible in the public portal are retained by the authors and/or other copyright owners and it is a condition of accessing publications that users recognise and abide by the legal requirements associated with these rights.

- Users may download and print one copy of any publication from the public portal for the purpose of private study or research.
- You may not further distribute the material or use it for any profit-making activity or commercial gain
- You may freely distribute the URL identifying the publication in the public portal

If you believe that this document breaches copyright please contact us providing details, and we will remove access to the work immediately and investigate your claim.

Multiscale Exploration of Texture and Microstructure Development in Recrystallization Annealing of Heavily Deformed Ferritic Alloys

C Yildirim¹, N Mavrikakis², P K Cook¹, R Rodriguez Lamas¹, H F Poulsen³, C Detlefs¹ and M Kutsal³

¹ European Synchrotron Radiation Facility, 38043 Grenoble, France

² OCAS, Pres. J.F. Kennedylaan 3, BE-9060, Zelzate, Belgium

³ Department of Physics, Technical University of Denmark, 2800 Kgs. Lyngby, Denmark

E-mail: can.yildirim@esrf.fr, mkutsal@fysik.dtu.dk

Abstract. We present a multi-scale study of recrystallization annealing of an 85% cold rolled Fe-3%Si-0.1%Sn alloy using a combination of dark field X-ray microscopy (DFXM), synchrotron X-ray diffraction (SXR), and electron backscatter diffraction (EBSD). Grains of interest from high stored energy (HSE) regions in a 200 μ m-thick sample are studied using DFXM during isothermal annealing. The intra-granular structure of the as deformed grain reveals deformation bands separated by $\approx 3\text{--}5^\circ$ misorientation. Geometrically Necessary Dislocation evolution during recrystallization and growth is investigated. These findings are supported by a quantitative non-destructive texture analysis using SXR in terms of pole figures and orientation distribution functions. Although no significant macroscopic texture change is observed up to 50% recrystallization, the calculated texture index indicates different nucleation and growth processes at various stages of annealing. Our results show that zones of local misorientation in the HSE regions are decisive for the formation and growth of recrystallized grains.

1. Introduction

Metal processing often includes steps during which the material is plastically deformed and new defects are introduced. The density and distribution of these defects not only determine the hardening in the deformed state, but also constitute the main driving force for annealing phenomena. Understanding the nucleation and growth of recrystallization in deformed materials therefore is of great industrial significance.

The experimental understanding of strengthening mechanisms, in the deformed state, and recrystallization has improved drastically over the past 30 years. Notably, with the introduction of electron backscatter diffraction (EBSD) in scanning electron microscopes, fast and automated data collection providing morphological and crystallographic information can be employed. Studies in the last decades have shown that the distribution of the recrystallized (RX) grains is highly influenced by the local deformation microstructure [1, 2]. However, although these studies improved our understanding of the dislocation structures, electron-based techniques have limited possibilities of dynamic studies within bulk material, due to their sample preparation requirements.

Within the past 20 years, synchrotron-based techniques such as 3D X-ray diffraction, or High Energy Diffraction Microscopy (3DXRD or HEDM) [3, 4], Diffraction Contrast Tomography (DCT) [5] and Differential Aperture X-ray Microscopy (DAXM) [6] have been used to investigate



recrystallization and growth phenomena in 3D and 4D (x, y, z, t). These studies have provided fascinating insights on the recrystallization and growth of near perfect grains within bulk materials. Yet, these methods fail to capture the multi-scale relation between the new nuclei and the highly deformed matrix due to limited spatial resolution and the peak overlap problem.

A relatively new synchrotron-based method called Dark Field X-ray Microscopy (DFXM) provides an alternative approach to the above-mentioned challenges. DFXM is a recently-developed diffraction imaging method for probing 3D nanostructures with their associated strain and orientation in bulk materials, with better angular resolution than its electron counterparts [7, 8]. An important feature of the microscope is that it can be coupled with coarser grain mapping methods such as 3DXRD and DCT without having to dismount the sample. Although at high deformation levels grain indexing is not possible, a quantitative texture analysis can still be carried out using the observed intensities from Debye-Scherrer rings. It has been shown that XRD is a well-suited tool for non-destructive texture characterization [9, 10]. Combining synchrotron XRD (SXR) texture information with DFXM data provides not only a volume-averaged understanding of the sample, but also the fine details of the intricate physics of a grain of interest (GOI) in micro scale within bulk.

Here, we explore the multi-scale links between the deformed state, recrystallization and grain growth using DFXM, SXR and EBSD upon annealing of a highly deformed ferritic alloy. We employ a texture analysis using pole figures (PFs) and orientation distribution functions (ODFs) from the SXR data to get an overall picture of the texture evolution. We investigate the evolution of microstructure in terms of GND density using the DFXM data.

2. Experimental

2.1. DFXM

The DFXM experiments were carried out at beamline ID06 at the European Synchrotron Facility (ESRF) [11]. A Si monochromator was used to select 33 keV photons. A set of 1D compound refractive lenses (CRLs) were used to obtain a line-focused beam. A far-field FReLoN CCD was positioned to image the (110) reflection of the grain. An X-ray objective comprising 2D CRLs was used to magnify the diffracted signal from the 2D slices of a GOI, which was projected onto the far-field detector with $\approx 90\text{nm}$ effective pixel size. The DFXM images showing the 3D structure of the GOI were then obtained by moving the sample in the z direction across the 1D condensed beam (figure 1(a)). The local crystallographic orientation, i.e. local 110 pole figure, was measured by scanning one (ω) or two (ω, χ) sample axes at a fixed scattering angle (2θ) (figure 1(a)). More details about the experimental setup can be found in [12]. The collected DFXM data were used to generate center-of-mass (COM) maps using the intensity at a pixel coordinate as function of the goniometer angles across the scan [13].

2.2. SXR

For the SXR experiments (figure 1(a)), a FReLoN CCD 2D detector was used having $47.3\ \mu\text{m}$ pixel size positioned at 170 mm from the sample, at beamline ID06. $500 \times 500\ \mu\text{m}^2$ -sized box beam with 33keV photon energy illuminated the sample while ω was rotated 360° in 1° steps. This configuration enabled complete coverage of the first two Debye-Scherrer rings, 110 and 200, and partial coverage (65° out of 360°) of the third ring, 211. The collected SXR patterns were pre-processed for background subtraction and distortion correction. The respective experimental geometries were calibrated using pyFAI software [14]. In order to derive a polar intensity distribution of the observed diffraction signal, the processed SXR patterns were averaged in 5° bins in ω -direction. The ω -averaged images were further divided to 5° slices in azimuthal direction, η , and subjected to 1D azimuthal integration with pyFAI software. The resulting polar intensity distributions were corrected for Lorentz and polarization factors [9, 15]. These distributions were used to derive pole figures (PFs) and orientation distribution functions

(ODFs) using MTEX software [16]. For the ODF derivation, the resolution of the associated Fourier transform was set as 5° . The derived ODFs were further utilized for re-evaluation of the PFs and for calculation of inverse pole figures (IPFs).

2.3. EBSD

Global recrystallization tendencies were followed with EBSD in the as deformed condition and after interrupted annealing in a dilatometer at 600°C . More details about the EBSD measurements can be found in [12].

2.4. Samples and Sample Environments

We studied Fe-3%Si-0.1%Sn samples that were hot rolled and annealed having a final average grain size of $100\ \mu\text{m}$ [17]. These samples were then cold rolled at a Von Mises true strain of about $\epsilon = 2$, corresponding to 85% reduction in size. The samples remain ferritic due to the high Si content of the alloy. Details of sample preparation is given elsewhere [12, 17]. Different samples from the same batch were used for the EBSD and synchrotron experiments. A hot air blower positioned 5 mm from the sample was used to perform the isothermal annealing steps for the synchrotron annealing studies. A total of 1432 s of isothermal heating at $\approx 610^\circ\text{C}$ was applied in 6 intermittent steps, achieving a global recrystallization amount of $\approx 50\%$ [18]. All X-ray measurements were then done at room temperature after air cooling.

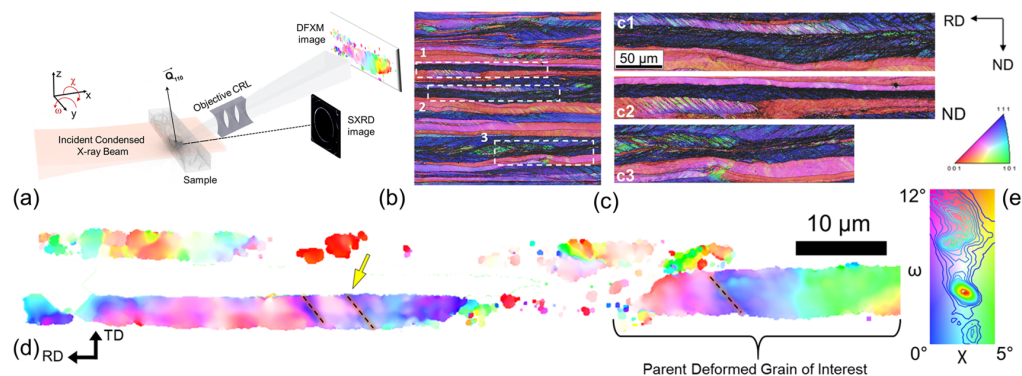


Figure 1. (a) Schematics of DFXM and SXRD setup. The GOI is shown darker. (b) EBSD Normal Direction-Inverse Pole Figure (ND-IPF) map of the initial microstructure of the as deformed state through thickness. (c) Zoom in on regions of high dislocation density. (d) DFXM mosaicity map of a selected layer of the deformed state. (e) The local 110 pole figure color key of the two sample tilts.

3. Microstructure of the Deformed State

Metals that are highly deformed typically exhibit a strongly textured microstructure and heterogeneous stored energy. Figure 1(b-c) shows the EBSD normal direction (ND) IPF superimposed on the image quality (IQ) mappings of the as deformed state. Deformation features such as transition bands (i.e. shear bands, deformation bands) are present. The deformed microstructure shows a rolling texture manifested by the marked appearance of α -fibre ($\{hkl\}\langle 110\rangle$), blue-red-magenta colored regions in (ND-IPF) and γ -fibre ($\{111\}\langle uvw\rangle$), blue regions in ND-IPF) [19]. In conventional cold rolled bcc metals, $\{111\}\langle uvw\rangle$ regions have the highest Taylor factor, with high stored energy (HSE) [20]. As a result, these HSE regions typically produce the first RX grains during the early stages of annealing [21–23]. We, therefore, focused on these HSE regions and mapped the 3D orientation of one using DFXM. An example of a typical DFXM mosaicity map of a given layer of the GOI in the deformed state is shown in figure 1(d). High spatial and angular resolution of DFXM uncovers the fine details of the deformed microstructure of GOI, located in the HSE regions. These details include deformation bands (e.g. yellow arrow) and cells having $<1^\circ$ misorientation across the stretched grain. The orientation gradients along the rolling direction separates zones with different substructure.

Notice that DFXM maps show intensity of the diffracting lattice, and the overall angular spread of the measured deformed grains exceeds 10° . Parts of the sample where the orientation falls outside of the scan range appear empty in the mosaicity maps.

4. Texture Analysis at the Deformed State

Figure 2(a) shows the SXR measured PFs of 110, 200 and 211 rings. A stronger signal in 110 and 200 PFs was observed with respect to 211 PF due to limited azimuthal coverage of the 211 ring. In order to compare the obtained SXR PFs to its EBSD-counterpart, the derived SXR PFs re-aligned to the EBSD geometry by rotating them with the appropriate angular relations between EBSD and SXR/DFXM experimental geometries. Therefore, the directions with respect to rolling measured by SXR correspond to that of the EBSD results. TD and RD IPFs are shown in figure 2(b), displaying 111 and 110 tendencies, respectively. Figure 2(c) shows sections of derived ODFs. The expected cold rolled bcc texture is observed (with α - and γ -fibre) when comparing the 45° ODF section to previous findings [24, 25]. In order to validate our

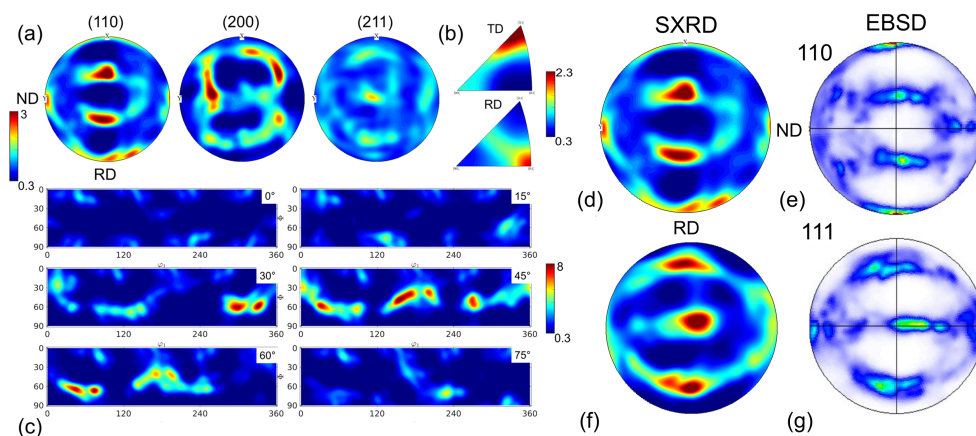


Figure 2. Texture in the as deformed state shown by (a) SXR Pole Figures. (b) Inverse Pole Figures (c) Orientation distribution functions (ODFs) serial sections of 15° at ϕ_2 of the 3D Euler space (Bunge's notation). 110 and 111 pole figures obtained by SXR (d, f) and EBSD (max. at 12 mrd) (e, g) measurements. All SXR pole figures have the same color scale.

SXR results, we compare the texture of the as deformed state with the EBSD PFs. Fig 2(d-g) shows this comparison of the SXR and EBSD measured 110 and 111 PFs. For both methods, the observed poles, peak position and relative intensities are in good agreement. Discrepancies between these maps can be attributed to the probed volume differences (i.e. limited penetration depth of EBSD compared to SXR). A detailed comparison of EBSD and XRD texture analysis in general is discussed elsewhere [24].

Looking at the 111 PFs (figure 2 (f-g)), one can notice that a 111 pole lies almost in the center. The other 111 poles have angles of 60° to 90° between them. According to the angles between 111 planes, the dominant texture can be found as $\{111\}\langle 112 \rangle$ -type texture [25], which is a common rolling texture of ferritic alloys. Both SXR and EBSD results show similar orientation relations with different intensity levels.

5. Texture Evolution Upon Annealing

Having established the texture in the deformed state, we can now focus on the effect of isothermal annealing on texture. Figure 3(a-f) show the SXR 111 PFs at different stages of annealing at 610°C . At a first glance, the overall orientation relations remain the same even at 50% recrystallization, in line with our previous work showing variance maps of the diffraction rings [12]. Nevertheless, 111 PFs show subtle changes upon annealing. In particular, a noticeable

decrease of intensity is observed when PFs of the as deformed state and the later stages of annealing are compared. Moreover, a gradual rotation of the texture peak is observed by $\approx 22^\circ$ counter clockwise for one of the 111 poles, figure 3(f) (noticeable at the upper hemisphere of PFs).

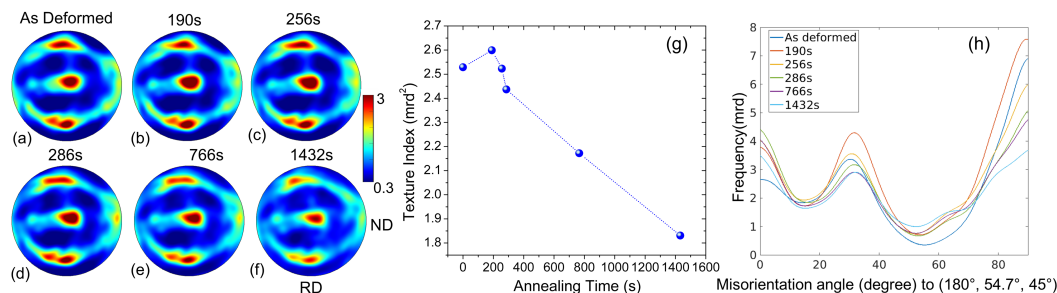


Figure 3. Evolution of 111 Pole Figures measured using SXRD (a-h). Intensity scales are identical for each pole figure. Calculated texture index as a function of annealing time at 610°C (g). Texture density along the γ -fibre (180-270°, 54.7°, 45°) with annealing time (h).

Interestingly, the 111 pole along the ND, towards $\langle 112 \rangle$ increases intensity up to 2.5 mrd from the as deformed state to 286s of annealing. Further annealing results in a continuous decrease of this texture component. Figure 3(g) shows the calculated texture index as a function of annealing time. The texture index is calculated using the following relation:

$$t = \int f(g)^2 dg \quad (1)$$

where $f(g)$ is the ODF [26]. There is an increase in the texture index at the early stages of annealing. Upon further annealing texture index decreases in two fashions: from 190s to 286s, a slope of $-0.0016 \text{ mrd}^2/\text{s}$ is read. Further annealing results in a slope change to $-0.00053 \text{ mrd}^2/\text{s}$, indicating the different effects of simultaneous recrystallization and grain growth.

From the calculated ODFs, we can focus on a specific texture component of the system and monitor its evolution upon annealing. Figure 3(h) shows the texture density along the γ -fibre with annealing. The peak position at around 30° remains almost the same with annealing. However, there is an increase of frequency of this texture component from the as deformed state to the early stages of annealing, at 190s, similar to what is observed in evolution of the texture index. This may be explained as the HSE regions give birth to many new nuclei during the early stages of annealing before the lower stored energy (LSE) regions can recrystallize. Since these new grains have similar orientation to their parents [12], they contribute to the overall HSE-zone texture, thus increasing the texture index. As recrystallization proceeds, the frequency of the γ decreases continuously, in line with the observed 111 PF intensity drop. This is because the LSE regions start to recrystallize. Hence, the advancement of recrystallization results in an overall texture softening.

6. GND Evolution Upon Annealing

After having established the meso-scale texture evolution, we now zoom into the parent GOI located in a HSE region shown in Fig 1(d), and monitor the GND evolution upon recrystallization and grain growth. Upon plastic deformation, GND density increases accommodating the lattice curvature and manifesting itself with a measurable local intragranular misorientation [27–29]. From mosaicity maps (Fig 1(d)), one can calculate the intragranular misorientation. The misorientation is defined by $\Delta\gamma = \sqrt{(\Delta\omega)^2 + (\Delta\chi)^2}$ [12]. Here, $\Delta\omega$ and $\Delta\chi$ are the differences between the local sample tilt COM and their grain averages. Considering the case of a lattice deformation proposed by [30], one can calculate the GND density using the following equation:

$$\rho_{GND} = \frac{\alpha \Delta \gamma}{bx} \quad (2)$$

where γ is the misorientation angle, α is a constant ($\alpha = 2$ for tilt misorientation [31]), b is the Burger's vector, and x is unit length.

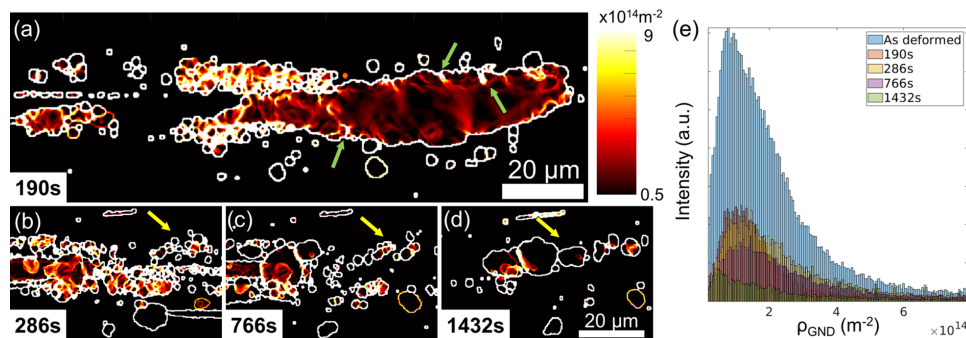


Figure 4. Generated GND density maps during different steps of annealing. (a) shows the early stages of the recrystallization, annealed at 190s at 610°C . (b-d) are zoomed-in views of the same area on the sample showing the recrystallization and growth competition along the further stages of annealing – all figures have the same color scale. (e) GND density distribution histograms at different heating steps.

Figure 4(a-d) shows the generated GND maps of given layers of the GOI at different annealing times. At 190s, we can observe a partially RX structure with new nuclei having formed within and around the deformed parent grain. The deformed parent grain still displays an angular spread larger than 8° , with considerably recovered zones. The regions with higher GND density corresponds to the junction points of the deformation bands (green arrows), and the boundaries of the newly-formed grains, reaching up to values $9 \times 10^{14} \text{m}^{-2}$. Similar values were reported for the same material [17] and on 92% cold-rolled Tantalum using EBSD [31]. The new nuclei, however, show ultra-fine structure with orientation spread $< 0.05^\circ$. The lower orientation spread is manifested by the low dislocation density, below 10^{13}m^{-2} . The new grains form around the bands and the prior grain boundaries of the as deformed parent grain. This is in line with the literature that the misorientation across the boundaries provides the driving force for recrystallization [32]. These regions are marked as high-strain regions in the as deformed structure, reaching up to measured axial strain values above 0.002 with elastic stored energy values larger than 10^4J/m^3 (not shown here). Further annealing causes grain growth (GG) of the RX grains. They grow at the expense of the remaining deformed matrix. The deformed matrix is progressively consumed by the new nuclei, while some of the already-nucleated grains grow. In particular, the growth competition between some RX grains can be monitored: at 286s, more than 15 RX grains having a size of $< 2 \mu\text{m}$ are observed (yellow arrow), whereas this number decreases down to 8 grains at 1432 s. GND density continues to decrease during this process. The growth rates of selected grains from the mosaicity maps were analyzed between 286 and 1432s of annealing. The growth rate appears to be size dependent, with values between 0.001 and $0.006 \mu\text{ms}^{-1}$. This difference in growth rate can be attributed to grain impingement; certain individual grains consume the non-RX matrix as they grow freely, while some impinge with other nuclei. The DFXM-calculated growth rates were compared with previous global observations of the same material [18]. These observations were done using optical microscopy (OM) and EBSD analyses after interrupted annealing. There, the mean growth rates were estimated as $0.015 \mu\text{ms}^{-1}$ for 650°C , $0.11 \mu\text{ms}^{-1}$ for 700°C , $0.71 \mu\text{ms}^{-1}$ for 750°C , respectively. The DFXM growth values during recrystallization correlate well with that of OM/EBSD considering the grain boundary velocity is proportional to the annealing temperature.

Finally, a general picture of the evolution of average GND density distribution upon annealing of the GOIs is shown in Fig 4(e). The large intensity drop between the as deformed and 190s

of annealing is due to the combined recovery and recrystallization effect, as the dislocations annihilate during recovery process. Further annealing results in a continuous decrease of the GND density with a slower rate, combining the effects of recrystallization and grain growth.

7. Conclusions and Outlook

We presented a multi-scale investigation of the microstructure and texture evolution of a heavily deformed (85%) ferritic alloy upon isothermal annealing, using a combination of DFXM, SXR D and EBSD methods. The SXR D texture analyses agree well with the EBSD results, showing a typical rolling texture observed in ferritic alloys. Although there are no significant texture changes up to 50% recrystallization, SXR D results reveal quantifiable subtle, but meaningful, variations at different steps of annealing. The evolution of the GND structure with annealing illustrate the coupled effects of recovery, recrystallization and grain growth. Combined with SXR D, DFXM can be a powerful technique to resolve subgrain dynamics and along with texture information can offer a new perspective in the study of recrystallization.

Acknowledgments

The authors acknowledge the ESRF for provision of beamtime at ID06. N.M. acknowledges the financial support of the National Association of Research and Technology (ANRT – Project no.1073–2015). HFP acknowledges support from ERC Advanced Grant nr 885022 and from the Danish ESS lighthouse on hard materials in 3D, SOLID. M.K. thanks Dr. M. Hazar Şeren for his valuable discussions on the development of the SXR D data analysis routine.

References

- [1] Xu W, Quadir M and Ferry M 2009 *Metall. Mater. Trans. A* **40** 1547–56
- [2] Zhang Y, Juul Jensen D, Zhang Y, Lin F, Zhang Z and Liu Q 2012 *Scr. Mater.* **67** 320–323
- [3] Schmidt S, Nielsen S F, Gundlach C, Margulies L, Huang X and Jensen D J 2004 *Science* **305** 229–32
- [4] Hefferan C M e a 2012 *Acta Mater.* **60** 4311–18
- [5] Sun J, Yu T, Xu C, Ludwig W and Zhang Y 2018 *Scr. Mater.* **157** 72–75
- [6] Xu C, Zhang Y, Godfrey A, Wu G, Liu W, Tischler J Z, Liu Q and Juul Jensen D 2017 *Sci. Rep.* **7** 1–7
- [7] Simons H *et al.* 2015 *Nat. Commun.* **6** 6098
- [8] Poulsen H F, Jakobsen A, Simons H, Ahl S R, Cook P and Detlefs C 2017 *J. Appl. Cryst* **50** 1441–56
- [9] Yuan H, Chen Z, Buslaps T, Honkimäki V and Borbély A 2018 *J. Appl. Cryst.* **51** 883–94
- [10] Sinclair C W *et al.* 2003 *Adv. Eng. Mater.* **5** 570–74
- [11] Kutsal M *et al.* 2019 *IOP Conf. Mat. Sci. and Eng.* **580** 012007
- [12] Yildirim C *et al.* 2022 *Scr. Mater.* **214** 114689
- [13] Ferrer Garriga J *et al.* 2022 *arXiv preprint: 2205.05494*
- [14] Ashiotis G *et al.* 2015 *J. Appl. Crystallogr.* **48** 510–519 ISSN 1600-5767
- [15] Poulsen H 2004 *Three-Dimensional X-Ray Diffraction Microscopy (Springer Tracts in Modern Physics vol 205)* (Germany: Springer Berlin Heidelberg)
- [16] Bachmann F, Hielscher R and Schaeben H 2010 *Solid State Phenom.* **160** 63–68
- [17] Mavrikakis N e a 2019 *Acta Mater.* **174** 92–104
- [18] Mavrikakis N *et al.* 2018 *IOP Conf. Ser.: Mater. Sci. Eng.* vol 375 (IOP Publishing) p 012016
- [19] Hoelscher M, Raabe D and Luecke K 1991 *Steel Res* **62** 567–75
- [20] Dillamore I L and Katoh H 1974 *Metal Science* **8** 73–83
- [21] Doherty R D *et al.* 1998 *Materials Today* **1** 14–15
- [22] Inagaki H 1994 *ISIJ International* **34** 313–321
- [23] Hutchinson W B 1984 *Int. Metals Rev.* **29** 25–42
- [24] Wright S I, Nowell M M and Bingert J F 2007 *Metall. Mater. Trans. A* **38** 1845–55
- [25] Fu J 2021 *J. Mater. Res. Technol.* **14** 1284–91
- [26] Hielscher R and Schaeben H 2008 *J. Appl. Cryst.* **41** 1024–37
- [27] Ashby M 1970 *Phil. Mag.* **21** 399–24
- [28] Nye J F 1953 *Acta Metal.* **1** 153–162
- [29] Gao H and Huang Y 2003 *Scr. Mater.* **48** 113–18
- [30] Kubin L and Mortensen A 2003 *Scr. Mater.* **48** 119–125
- [31] Moussa C, Bernacki M, Besnard R and Bozzolo N 2015 *IOP Conf. Ser.: Mater. Sci. Eng.* vol 89 p 012038
- [32] Humphreys F J and Hatherly M 2004 *Recrystallization And Related Annealing Phenomena* 2nd ed (United Kingdom: Elsevier Science)